Synthesis of hierarchical mesoporous nest-like $Li_4Ti_5O_{12}$ for high-rate lithium ion batteries

Jizhang Chen [a], Li Yang [a,*], Shaohua Fang [a], Shin-ichi Hirano [b], Kazuhiro Tachibana [c]

[a] *School of Chemistry and Chemical Engineering, Shanghai Jiaotong University, Shanghai 200240, China*
[b] *Hirano Institute for Materials Innovation, Shanghai Jiaotong University, Shanghai 200240, China*
[c] *Department of Chemistry and Chemical Engineering, Faculty of Engineering, Yamagata University, Yamagata 992-8510, Japan*

ABSTRACT

Hierarchical mesoporous nest-like $Li_4Ti_5O_{12}$ is prepared by a hydrothermal reaction, using CTAB as the surfactant, and water-soluble titanium complex $[NH_4^+]_4[H^+]_2[Ti_4(C_2H_2O_3)_4(C_2H_3O_3)_2(O_2)_4O_2]^{6-}$ as the titanium precursor. As-prepared $Li_4Ti_5O_{12}$ has a tiny crystallite size of 8.2 nm and a very large surface area of 219.2 $m^2\,g^{-1}$. Commercial micrometer-sized $Li_4Ti_5O_{12}$ is also tested for comparision, and up to 10 000 $mA\,g^{-1}$ (57 C) is applied to evaluate these two samples as the anode material for lithium ion batteries. Our products deliver much better cycling and rate performances, especially at high current densities. 135.1 $mAh\,g^{-1}$ is obtained after 200 cycles at 2500 $mA\,g^{-1}$, and 113.6 $mAh\,g^{-1}$ is obtained at 10 000 $mA\,g^{-1}$. The polarization in our products is much lower, and our products also show higher lithium diffusion coefficient and higher exchange current density, calculated from CV and EIS measurements.

Crown Copyright © 2011 Published by Elsevier B.V. All rights reserved.

1. Introduction

Lithium ion batteries, as promising power sources for portable electronics and zero- or low-emission pure or hybrid electric vehicles, have attracted tremendous interest [1,2]. However, the power density and safety of current lithiun ion batteries are too low to satisfy future high rate applications. Graphite, a commonly used anode material, has small lithiun diffusion coefficient and experiences large volune variation of 9% in the lithium insertion–extraction process. In addition, it has severe safety issues of dendritic lithium growth, due to its low operating voltage (below 0.2 V versus Li+/Li). Especially at high rates, the polarization would considerably lower its operating voltage, causing safety issues, and thick SEI layer on the surface of graphite could also bring in kinetic problems. $Li_4Ti_5O_{12}$ spinel (*Fd3m*), viewed as an alternative anode material to carbon-based materials, has been found to change its structure negligibly during the discharge/charge process, and possess good lithium ion mobility and a long and stable voltage plateau at approximately 1.5 V versus Li+/Li, together with low cost, environmental friendliness, and enhanced safety [3–6]. However, the intrinsic low electronic conductivity of bulk $Li_4Ti_5O_{12}$ (merely $10^{-13}\,S\,cm^{-1}$) restricts its high rate performance, and coating with conductive materials (e.g., carbon, TiN, and Ag) [7–13], doping with

other metals (e.g., Mg^{2+}, Al^{3+}, Cr^{3+}, Ni^{3+}, V^{5+}) [14–17], and nanotechnology have been proposed trying to overcome this obstacle.

Decreasing the particle size of $Li_4Ti_5O_{12}$ to nanoscale is an effectual method, since the diffusion length of e− is significantly reduced, and consequently its low electronic conductivity is no longer a serious obstacle. Using hydro-/solvothermal methods, nanostructured $Li_4Ti_5O_{12}$ with various morphologies such as nanowires, nanotubes, nanorods, nanosheets, and nanoparticles have been prepared and exhibit improved cycling and rate performances, compared to bulk $Li_4Ti_5O_{12}$ [18–23]. Unfortunately, nanosized materials are prone to agglomerate during electrochemical cycles, leading to rapid capacity decay. A strategy to solve this problem is to design hierarchical structure, which possesses both the merits of nanometer-sized building blocks (e.g., shortened diffusion distance and high surface area) and micro- or submicrometer-sized assemblies (e.g., thermodynamic stability and high tap-density), and superb cycling and rate performances have been obtained by fabricating such structure [24–28]. The hierarchical structure could also provide porous structure [12,26]. The electrolyte can easily penetrate into porous structure, then the transportation of solvated Li+ is facile. And Li+ can also be captured in the pores, benefiting for specific capacity.

In this work, hierarchical mesoporous nest-like $Li_4Ti_5O_{12}$ was prepared by hydrothermal reaction of LiOH with water-soluble titanium complex $[NH_4^+]_4[H^+]_2[Ti_4(C_2H_2O_3)_4(C_2H_3O_3)_2(O_2)_4O_2]^{6-}$. Surfactant CTAB was employed as the template to obtain this hierarchical structure, and the effect of CTAB was investigated.

* Corresponding author. Tel.: +86 21 54749917; fax: +86 21 54741297.
E-mail address: liyangce@sjtu.edu.cn (L. Yang).

As-prepared $Li_4Ti_5O_{12}$ has a tiny crystallite size and a very large surface area. Commercial micrometer-sized $Li_4Ti_5O_{12}$ is also evaluated for comparision, and it delivered much worse rate performance than our products. Calculated from CV and EIS measurements, our products have higher lithium diffusion coefficient and higher exchange current density. Based on our experimental results, we think that much larger polarization would occur for commercial $Li_4Ti_5O_{12}$, and it suffer from very severe kinetic problems, especially at high rates. Our configuration of hierarchical mesoporous nest-like structure has proven itself effectual to solve these problems.

2. Experimental

2.1. Sample preparation and characterization

All chemicals were used as received. The water-soluble titanium complex was prepared according to literature methods [29]. Typically, 2 mmol titanium metal powder was added to an ice-cooled aqueous solution consisting of 8 mL 30% H_2O_2 and 2 mL 28% NH_3. After 3 h, 3 mmol glycolic acid was added, and this solution was heated at 80 °C with stirring for 6 h to remove excess H_2O_2 and NH_3, and form gel-like orange precursor. This precursor was dissolved in 20 mL aqueous solution containing 0.3 M CTAB and 0.5 M LiOH. After stirred for 1 h, the solution was transferred into a Teflon-lined stainless autoclave, which was maintained at 180 °C for 12 h and then cooled to room temperature naturally. The resulting white precipitate was recovered by centrifugation, washed with deionized water thoroughly, and then dried in an oven at 80 °C. Finally, the as-prepared sample was calcined in a muffle at 550 °C for 6 h in the air. The composition and crystal structure of the products were characterized by X-ray diffraction measurement (XRD, Rigaku, D/max-Rbusing Cu Kα radiation) and Raman spectroscopy (Bruker Optics Senterra R200-L with a laser at 633 nm). The morphology and microstructure were obtained using field emitting scanning electron microscopy (FE-SEM, JEOL JSM-7401F) and transmission electron microscopy (TEM, JEOL JEM-2010 equipped with Energy Dispersive X-ray Detector). The N_2 adsorption/desorption tests were carried out by Micromeritics ASAP 2010 instrument.

2.2. Electrode preparation and electrochemical characterization

Electrochemical measurements were performed using 2016-type coin cells assembled in an argon-filled glove box (German, M. Braun Co., $[O_2] < 1$ ppm, $[H_2O] < 1$ ppm). For preparing working electrodes, a mixture of the active material, acetylene black, and polyvinylidene fluoride (PVDF) binder at a weight ratio of 80:10:10 was pasted on pure copper foil. Pure lithium foil was used as the counter electrode. A glass fiber (GF/A) from Whatman was used as the separator. The electrolyte consisted of a solution of 1 M $LiPF_6$ in ethylene carbonate and dimethyl carbonate (EC + DMC) (1:1 in volume). The cells were cycled under different current densities between cutoff voltages of 2.5 and 1.0 V on a CT2001A cell test instrument (LAND Electronic Co.) at room temperature. Cyclic voltammetry (CV) and electrochemical impedance spectroscopy (EIS) were measured on a CHI660D electrochemical workstation.

3. Results and discussion

Fig. 1 shows low and wide angle XRD patterns of our products (denoted as PLTO) and commercial $Li_4Ti_5O_{12}$ (denoted as CLTO) obtained from Shenzhen BTR. It is seen that the wide-angle XRD profile of PLTO is in line with spinel $Li_4Ti_5O_{12}$ (JCPDS 49-0207), without the presence of impurities such as Li_2TiO_3, which usually exists in $Li_4Ti_5O_{12}$ prepared by hydrothermal reactions [26].
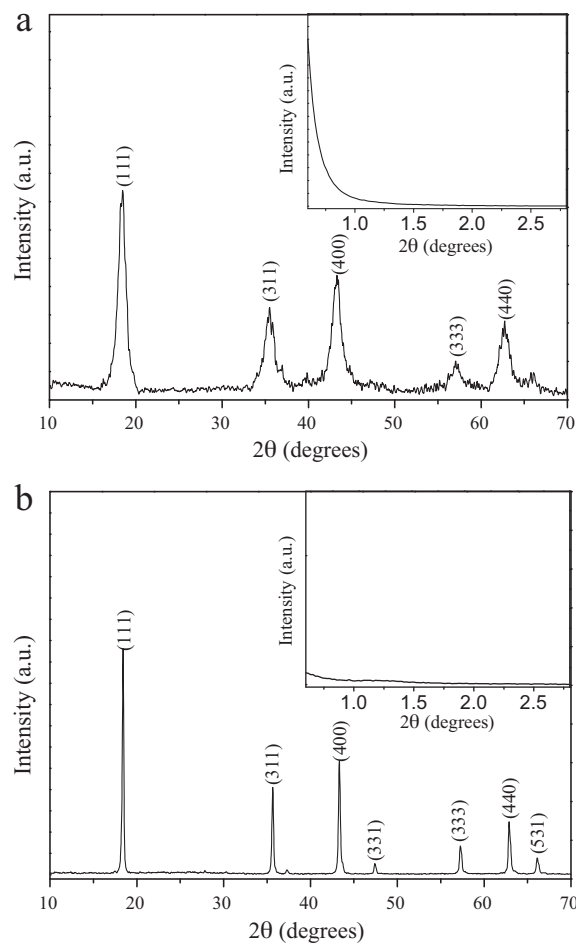

Fig. 1. Wide-angle and small-angle (inset) XRD patterns of (a) PLTO and (b) CLTO.

Notably, the wide-angle diffraction peaks of PLTO are much broader than CLTO, indicating that there is a large difference in the crystallite size. The mean crystallite sizes of PLTO and CLTO calculated from Scherrer's formula are ca. 8.2 and 50.7 nm, respectively. In addition, the low-angle XRD patterns suggest disordered mesoporous arrangement of PLTO and nonporous structure of CLTO.

Raman spectra of PLTO are shown in Fig. 2. Five vibration peaks at 227.8, 276.5, 334.5, 426.5, and 673.9 cm^{-1} representing the features of $A_{1g} + E_g + 3F_{2g}$ spinel structure can be observed [30,31].
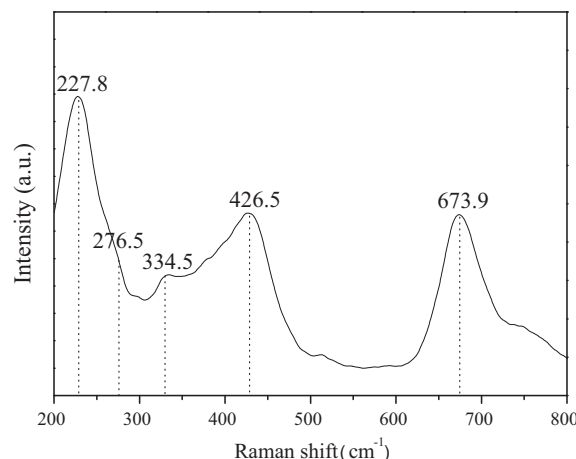

Fig. 2. Raman spectra of PLTO.

The peak at $673.9\,cm^{-1}$ is characteristic of A_{1g} mode, which can be ascribed to Ti–O stretches in "TiO_6" octahedral. The peak at $426.5\,cm^{-1}$ is assigned to E_g mode, and the other three peaks are F_{2g} modes.

As shown in Fig. 3, N_2 adsorption/desorption isotherms of PLTO reveal type IV isotherms with a representative H_1-type hysteresis loop, indicating the mesoporous nature, which can also be confirmed by Barrett–Joyner–Halanda (BJH) pore-size distributions (inset). Two well resolved narrow peaks centered at ca. 4 and 6 nm can be observed, with a total pore volume of $0.509\,cm^3\,g^{-1}$. According to Brunauer–Emmett–Teller (BET) analysis, the specific surface area is $219.2\,m^2\,g^{-1}$, much larger than $Li_4Ti_5O_{12}$ nanotubes, nanowires, nanosheets, and hierarchically porous microspheres, and is thus favor for lithium storage [20–22,26]. As for CLTO (Fig. 2b), the BET surface area and pore volume are merely $11.0\,m^2\,g^{-1}$ and $0.037\,m^3\,g^{-1}$, respectively.

Further structural characterization of our products was implemented by using SEM and TEM technologies. Fig. 4a displays a panoramic SEM micrograph of PLTO with rough surface and uniform morphology. In Fig. 4b, nest-like structure can be observed, and the thickness of the wall is 50–80 nm. TEM images in Fig. 4c and d reveal that our products possess hierarchical structure, i.e., mesoporous nest-like structure. We can clearly observe the porous
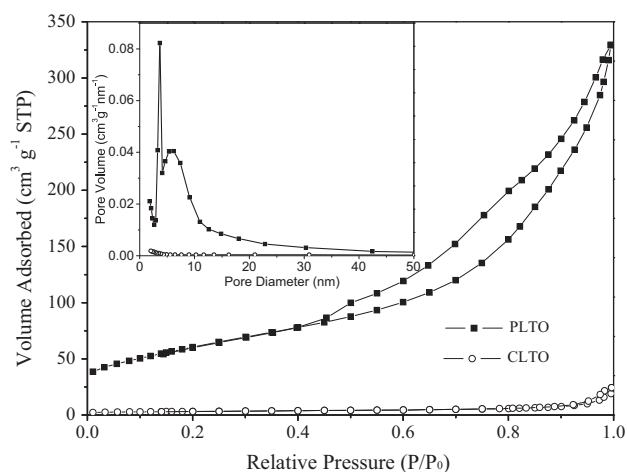

Fig. 3. N_2 adsorption and desorption isotherms of PLTO and CLTO. The inset shows corresponding BJH pore-size distributions.
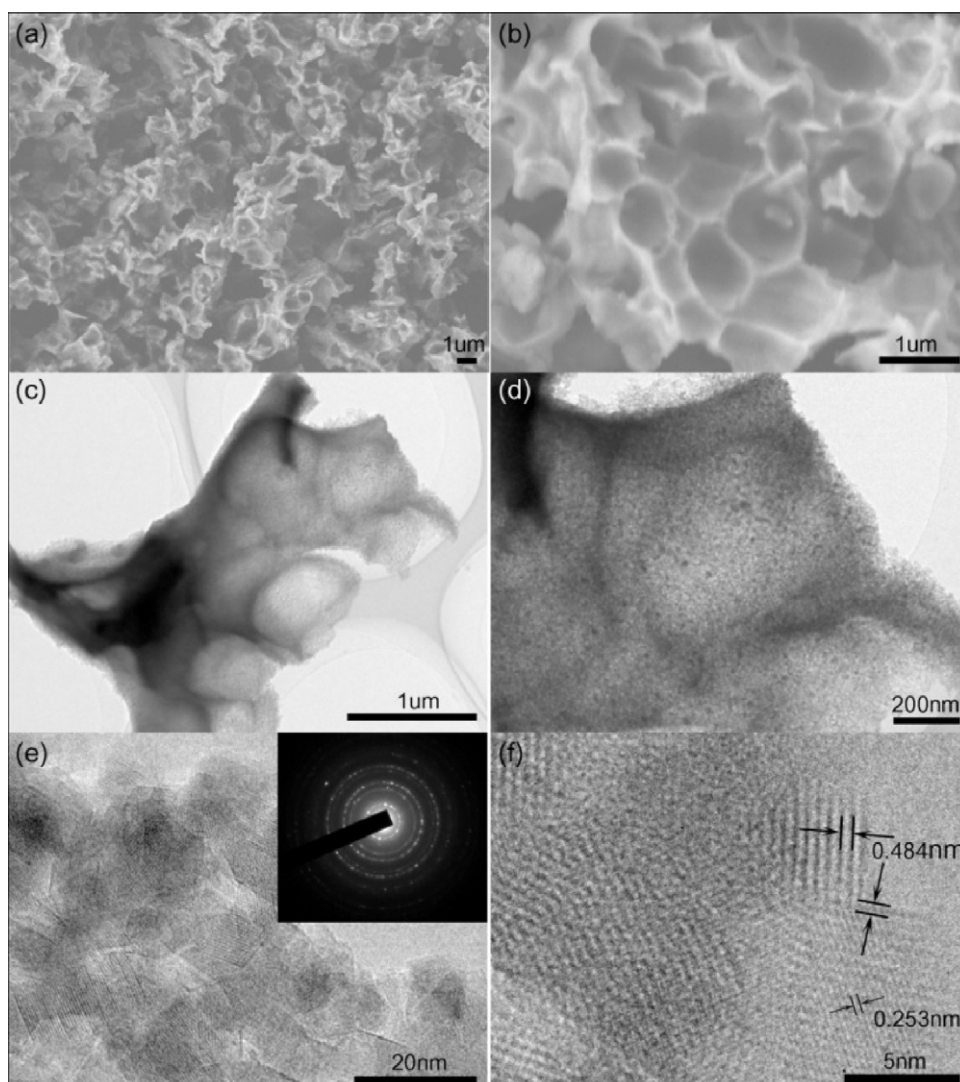

Fig. 4. SEM and TEM images of PLTO with different magnification (the inset shows SAED pattern).
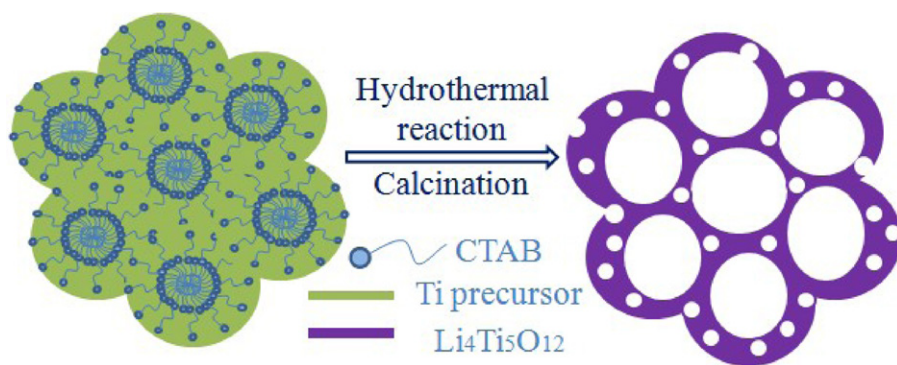
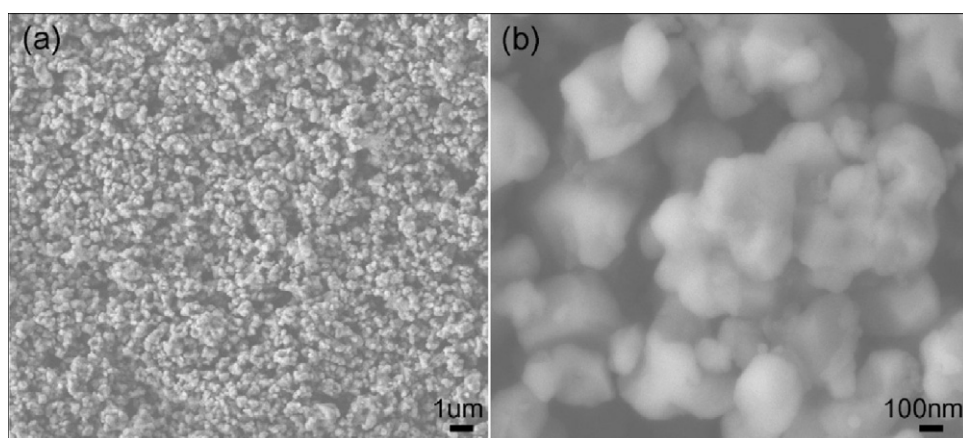**Fig. 5.** Schematic illustration of the fabrication process of PLTO.

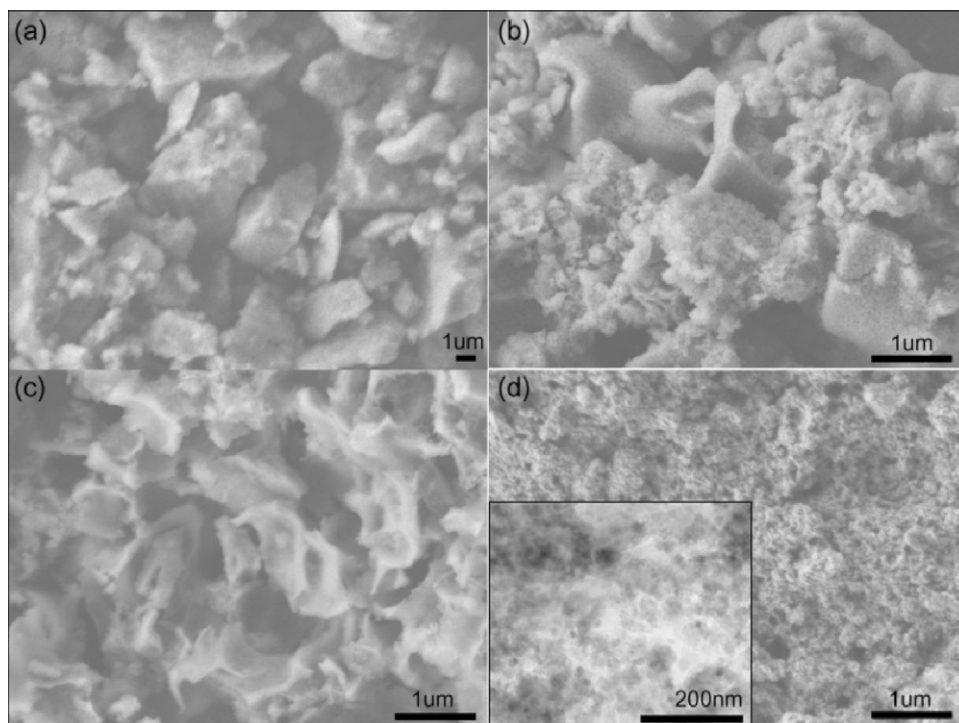**Fig. 6.** SEM images of CLTO.

Fig. 7. SEM images of our products when employing different concentrations of CTAB (a: 0 M, b: 0.1 M, c: 0.2 M, d: 0.5 M, the inset is TEM image of d).
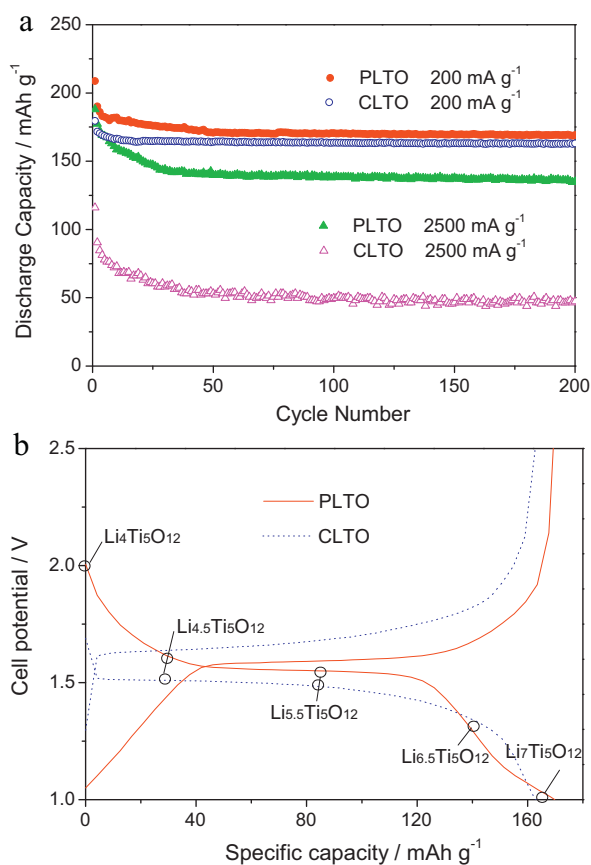
Fig. 8. (a) Cycle performances at different current densities and (b) discharge/charge curves of PLTO and CLTO after 200 cycles at 200 mA g^{-1} in the potential range of 2.5–1.0 V.

Fig. 9. (a) Rate performances of PLTO and CLTO from 200 mA g^{-1} to 10 000 mA g^{-1} and (b) galvanostatic discharge/charge curves at each rate.

structure in Fig. 4e. HRTEM image in Fig. 4f gives lattice fringes of 0.484 and 0.253 nm, corresponding to (1 1 1) and (3 1 1) interplanar spacing of $Li_4Ti_5O_{12}$, respectively. The inset SAED pattern, with several rings observed, can be indexed to spinel $Li_4Ti_5O_{12}$ with the cubic space group $Fd3m$. The schematic illustration of our products is shown in Fig. 5, where template CTAB was sacrificed via calcination and mesoporous nest-like structure was formed. In the case of CLTO (Fig. 6), it is micrometer-sized particles.

CTAB as the template plays a significant role in the formation of hierarchical mesoporous nest-like structure. The addition of CTAB would not make the synthesis procedure become complex, since CTAB can be easily removed via the calcination at 550 °C, which is an essential step to convert layered hydrous lithium titanate obtained after hydrothermal reaction to the final product $Li_4Ti_5O_{12}$ [21]. Fig. 7 shows SEM images of $Li_4Ti_5O_{12}$ when employing different concentrations of CTAB. When no CTAB was added, big particles were obtained (Fig. 7a). When the concentrations of CTAB increased to 0.1 and 0.2 M, nest-like structure (0.3 M) gradually formed. If 0.5 M CTAB was added, the nest-like structure disappeared, and instead, dispersed small particles were obtained.

The electrochemical properties of $Li_4Ti_5O_{12}$ were studied by galvanostatic method using $Li_4Ti_5O_{12}$/Li half cells. Fig. 8a shows cycling performances of PLTO and CLTO at 200 and 2500 mA g^{-1}. At 200 mA g^{-1}, PLTO delivered discharge capacities of 208.7 and 169.2 mAh g^{-1} at 1st and 200th cycles respectively. The capacity dropped manly for initial 50 cycles, and then the capacity retention was superb, with capacity loss of merely 2 mAh g^{-1} from 50th to 200th cycles. As for CLTO, it also gave great capacity retention and 163 mAh g^{-1} was obtained after 200 cycles at 200 mAh g^{-1}. We can see that PLTO has a larger initial capacity than CLTO, and this
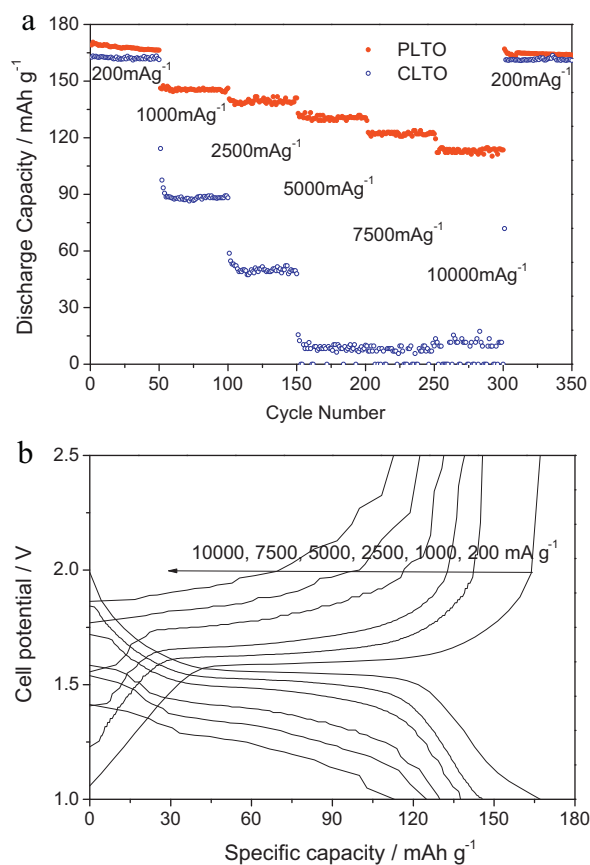
originates from mesoporous structure of our products, which can provide extra location to store lithium. The large initial capacity loss of PLTO could be attributed to irreversible lithium storage of mesoporous structure, surface defects such as surface vacancies or voids, and adsorbed trace water, which is a common phenomenon of nanosized materials. When the current density was increased to 2500 mA g^{-1}, the discharge capacities after 200 cycles were 135.1 and 47.3 mAh g^{-1} for PLTO and CLTO respectively, manifesting that our products have much better cycling performance at high current density. The discharge/charge curves of PLTO and CLTO after 200 cycles at 200 mA g^{-1} are presented in Fig. 8b. There are distinct potential plateaus at ca. 1.55 (discharging curve) and 1.60 V (charging curve) for PLTO, associating to the two-phase equilibrium between $Li_4Ti_5O_{12}$ and $Li_7Ti_5O_{12}$ [11]. The potential plateaus of CLTO are ca. 1.50 and 1.68 V, with the potential interval being 0.18 V, much larger than 0.05 V of PLTO, indicating that much severer polarization occurs in CLTO.

After 200 galvanostatic cycles at 200 mA g^{-1}, rates of up to 10 000 mA g^{-1} have been investigated to further evaluate these two samples and the results are displayed in Fig. 9. The rate was increased stepwise to 10 000 mA g^{-1}, and finally back to 200 mA g^{-1}, ~50 cycles for each rate. The discharge capacities of PLTO in the last cycle at each rate were 168.6, 145.6, 139.0, 130.5, 122.1, 113.6 and 164.1 mAh g^{-1}. This rate capability is higher than hierarchically porous $Li_4Ti_5O_{12}$, and much higher than most reported $Li_4Ti_5O_{12}$ [26]. Comparatively, the rate performance of CLTO is very poor. When the rate was increased to 5000 mA g^{-1}, the discharge capacity was in the range of 0–10 mAh g^{-1}, whereas it returned back to 160.9 mAh g^{-1} when the rate was reduced to 200 mAh g^{-1}. This demonstrates that the mechanical integrity
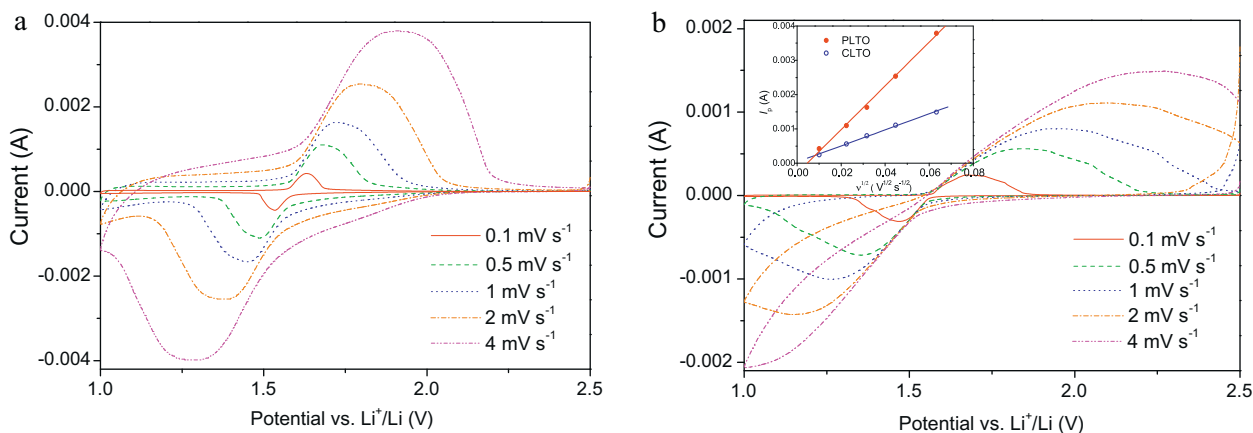
Fig. 10. Cyclic voltammograms of (a) PLTO and (b) CLTO at different scan rates after 200 cycles (inset of b: the relationships between the peak current and the scan rate in the anodic process for PLTO and CLTO).
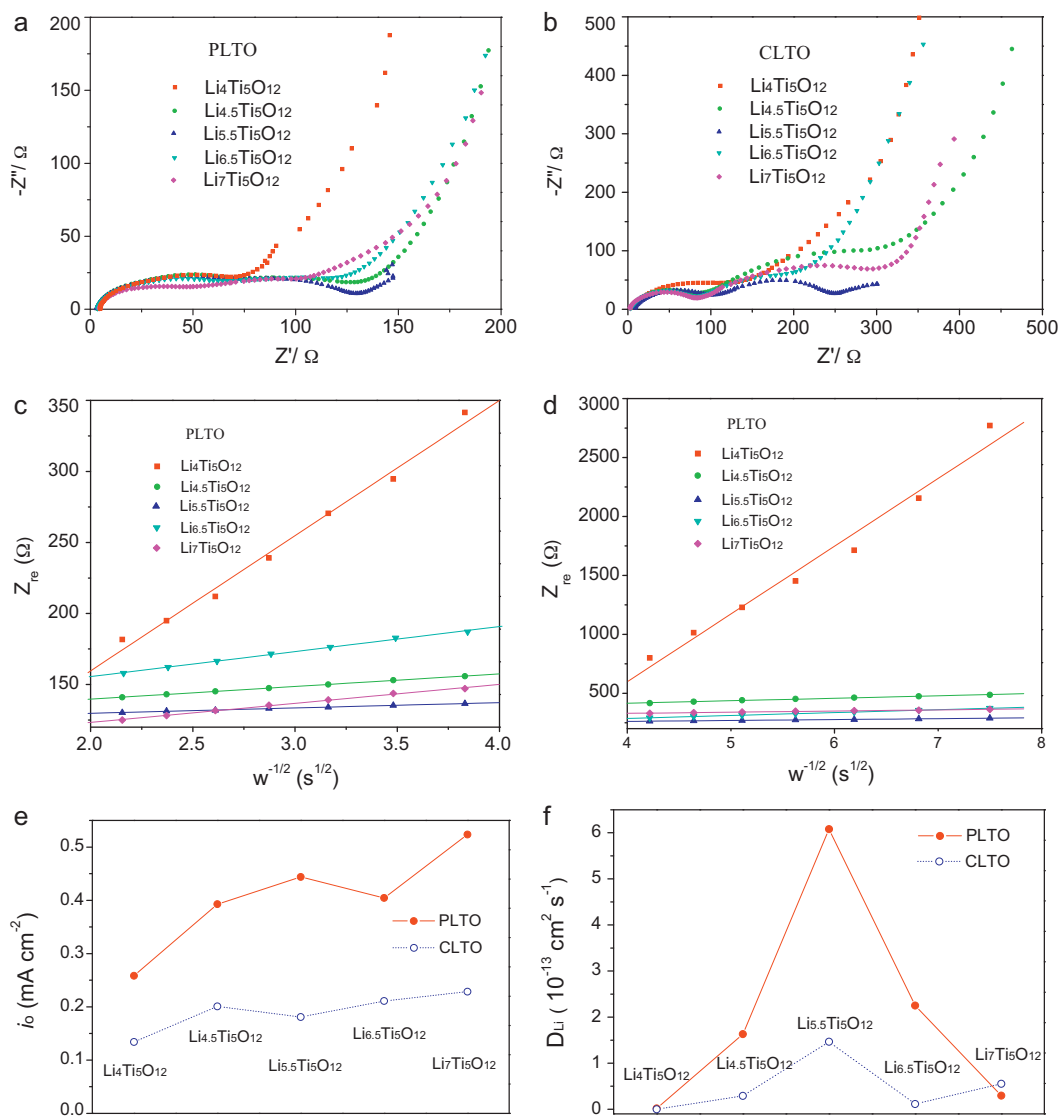

Fig. 11. (a, b) Nyquist plots, (c, d) dependence of Z_{re} with $w^{-1/2}$, (e) i_0, and (f) lithium ion coefficients D_{Li} of PLTO and CLTO at different discharge states after 200 galvanostatic cycles.

was also maintained at high rates for CLTO, but it suffers from severe kinetic problems. The superior electrochemical performances of our products PLTO are rooted in its intriguing structure, namely hierarchical mesoporous nest-like structure. On the one hand, the nest-like morphology as well as porous structure and very large surface area would make the active material contact with the electrolyte sufficiently enough, thus decreasing polarization significantly. On the other hand, tiny crystallite size would favor solid-state diffusions of both Li$^+$ and e$^-$, and micrometer-sized whole block could provide a thermodynamically stable system.

CV measurements conducted at different scan rates after 200 galvanostatic cycles are presented in Fig. 10 with cutoff voltages of 2.5–1 V (versus Li$^+$/Li). At 0.1 mV s^{-1}, one pair of apparent anodic/cathodic peaks located at 1.630 and 1.535 V can be observed for PLTO, accordingly well with the plateaus of the discharging/charging curves. The peak current increases with the scan rate, and the ratio of anodic to cathodic peak currents is nearly 1 even at 4 mV s^{-1}. And the anodic and cathodic curves are symmetrical throughout the measurements, demonstrating that the lithium storage is highly reversible and this redox system remains in equilibrium at a high scan rate. As for CLTO, the curves are highly anisomerous especially at high scan rates, and the peak current of PLTO is much larger than CLO. The potential interval ΔE between the anodic and cathodic peaks increases with the scan rate, and this is caused by the polarization. It is seen that ΔE of PLTO is much lower than CLTO, suggesting that much lower polarization occurred for PLTO, and this is why PLTO has a much higher rate capability. We can calculate the lithium diffusion coefficient based on Randles–Sevcik equation:

$$I_p = 2.687 \times 10^5 An^{3/2}C_{Li}D_{Li}^{1/2}v^{1/2} \ (25\,^\circ C) \tag{1}$$

In this equation, the peak current is in direct proportion to the square root of the scan root, agreeing with our results (inset of Fig. 10b), indicating solid phase diffusion-controlled process [25]. The lithium diffusion coefficients of PLTO and CLTO are calculated to be 2.58×10^{-11} and 3.47×10^{-12} cm^2 s^{-1}, implying that lithium diffusion in PLTO is more facile.

Electrochemical impedance spectroscopy (EIS) measurements were also carried out at different discharge states (Fig. 8b) in the frequency range from 100 000 to 0.01 Hz after 200 galvanostatic cycles, and typical Nyquist plots are given in Fig. 11a and b. The depressed semicircles at high/medium frequency are reflective of SEI impedance and charge transfer impedance R_{ct}, and the inclined lines at low frequency correspond to lithium diffusion within the active material. The exchange current densities i_0 of PLTO and CLTO based on the geometrical electrode area ($A = 1.5386$ cm^2) are listed in Fig. 11e, calculated according to this equation:

$$i_0 = \frac{RT}{nFR_{ct}A} \tag{2}$$

Obviously, the initial discharge state of Li$_4$Ti$_5$O$_{12}$ has the lowest i_0, and PLTO has a higher i_0 than CPLO. The lithium diffusion coefficients could also be calculated from the low frequency parts of EIS curves [32].

$$\sigma = \frac{RT}{n^2F^2A\sqrt{2}}\left(\frac{1}{C_{Li}D_{Li}^{1/2}}\right) \tag{3}$$

$$Z_{re} = R + \sigma w^{-1/2} \tag{4}$$

σ is the Warburg factor, Z_{re} is the real part of the impedance, ω is the frequency, and σ could be determined by the slope coefficient of Z_{re} to $\omega^{-1/2}$ (see Fig. 11c and d). The corresponding lithium diffusion coefficients D_{Li} of PLTO and CLTO are listed in Fig. 11f, where Li$_{5.5}$Ti$_5$O$_{12}$ has the highest D_{Li}, and this discharge state is at the center of the potential plateau. It is noted that D_{Li} in PLTO is higher. We

can also see that D_{Li} from EIS are about two orders of magnitude lower than that from CV, similar to LiFePO$_4$/C nanocomposite [33], probably because practical electrodes are in fact not theoretically planar electrodes.

4. Conclusions

In summary, we have synthesized hierarchical mesoporous nest-like Li$_4$Ti$_5$O$_{12}$ with a very large surface area by a hydrothermal reaction, using water-soluble titanium complex [NH$_4^+$]$_4$[H$^+$]$_2$[Ti$_4$(C$_2$H$_2$O$_3$)$_4$(C$_2$H$_3$O$_3$)$_2$(O$_2$)$_4$O$_2$]$^{6-}$ as the titanium precursor and CTAB as the surfactant. The effect of CTAB is investigated, and it would not make the fabrication procedure become complex. Our products delivered 135.1 mAh g^{-1} after 200 cycles at 2500 mA g^{-1} and 113.6 mAh g^{-1} at 10 000 mA g^{-1}, much better than commercial micrometer-sized Li$_4$Ti$_5$O$_{12}$. In addition, our products also show higher lithium diffusion coefficient and higher exchange current density, calculated from CV and EIS measurements. The improved cycling and rate performances of our products are attributed to the unique and intriguing morphology. The hierarchical configuration, porous structure, tiny crystallite size, and large surface area would considerably lower the polarization.

References

[1] M.R. Palacín, Chem. Soc. Rev. 38 (2009) 2565–2575.
[2] B. Scrosati, J. Garche, J. Power Sources 195 (2010) 2419–2430.
[3] K.M. Colbow, J.R. Dahn, R.R. Haering, J. Power Sources 26 (1989) 397–402.
[4] T. Ohzuku, A. Ueda, N. Yamamoto, J. Electrochem. Soc. 142 (1995) 431–1435.
[5] L. Kavana, M. Grätzel, Electrochem. Solid-State Lett. 5 (2002) A39–A42.
[6] H.K. Kim, S.M. Bak, K.B. Kim, Electrochem. Commun. 12 (2010) 1768–1771.
[7] H. Kitaura, A. Hayashi, T. Ohtomo, S. Hama, M. Tatsumisago, J. Mater. Chem. 21 (2011) 118–124.
[8] T. Yuan, X. Yu, R. Cai, Y.K. Zhou, Z.P. Shao, J. Power Sources 195 (2010) 4997–5004.
[9] L. Cheng, J. Yan, G.N. Zhu, J.Y. Luo, C.X. Wang, Y.Y. Xia, J. Mater. Chem. 20 (2010) 595–602.
[10] Y.G. Wang, H.M. Liu, K.X. Wang, H. Eiji, Y.R. Wang, H.S. Zhou, J. Mater. Chem. 19 (2009) 6789–6795.
[11] K.S. Park, A. Benayad, D. Joon Kang, S.G. Doo, J. Am. Chem. Soc. 130 (2008) 14930–14931.
[12] L. Zhao, Y.S. Hu, H. Li, Z.X. Wang, L.Q. Chen, Adv. Mater. 23 (2011) 1385–1388.
[13] S.H. Huang, Z.Y. Wen, J.C. Zhang, X.L. Yang, Electrochim. Acta 52 (2007) 3704–3708.
[14] C.H. Chen, J.T. Vaughey, A.N. Jansen, D.W. Dees, A.J. Kahaian, T. Goacher, M.M. Thackeray, J. Electrochem. Soc. 148 (2001) A102–A104.
[15] H.L. Zhao, Y. Li, Z.M. Zhu, J. Lin, Z.H. Tian, R.L. Wang, Electrochim. Acta 53 (2008) 7079–7083.
[16] T.F. Yi, J. Shu, Y.R. Zhu, X.D. Zhu, R.S. Zhu, A.N. Zhou, J. Power Sources 195 (2010) 285–288.
[17] D. Capsoni, M. Bini, V. Massarotti, P. Mustarelli, S. Ferrari, G. Chiodelli, M.C. Mozzati, P. Galinetto, J. Phys. Chem. C 113 (2009) 19664–19671.
[18] J.R. Li, Z.L. Tang, Z.T. Zhang, Electrochem. Commun. 7 (2005) 894–899.
[19] Y. Li, G.L. Pan, J.W. Liu, X.P. Gao, J. Electrochem. Soc. 156 (2009) A495–A499.
[20] J. Kim, J. Cho, Electrochem. Solid-State Lett. 10 (2007) A81–A84.
[21] J.Z. Chen, L. Yang, S.H. Fang, Y.F. Tang, Electrochim. Acta 55 (2010) 6596–6600.
[22] S.C. Lee, S.M. Lee, J.W. Lee, J.B. Lee, S.M. Lee, S.S. Han, H.C. Lee, H.J. Kim, J. Phys. Chem. C 113 (2009) 18420–18423.
[23] D. Fattakhova, V. Petrykin, J. Brus, T. Kostlánová, J. Dědeček, P. Krtil, Solid State Ionics 176 (2005) 1877–1885.
[24] S.H. Yu, A. Pucci, T. Herntrich, M.G. Willinger, S.H. Baek, Y.E. Sung, N. Pinna, J. Mater. Chem. 21 (2011) 806–810.
[25] L. Lai, Y.Y. Dou, X. Li, X.P. Gao, J. Power sources 195 (2010) 3676–3679.
[26] L.F. Shen, C.Z. Yuan, H.J. Luo, X.G. Zhang, K. Xu, Y.Y. Xia, J. Mater. Chem. 20 (2010) 6998–7004.
[27] Y.G. Guo, J.S. Hu, L.J. Wan, Adv. Mater. 20 (2008) 2878–2887.

[28] A.M. Cao, J.S. Hu, H.P. Liang, L.J. Wan, Angew. Chem. Int. Ed. 44 (2005) 4391–4395.
[29] K. Tomita, V. Petrykin, M. Kobayashi, M. Shiro, M. Yoshimura, M. Kakihana, Angew. Chem. Int. Ed. 45 (2006) 2378–2381.
[30] L. Aldon, P. Kubiak, M. Womes, J.C. Jumas, J. Olivier-Fourcade, J.L. Tirado, J.I. Corredor, C.P. Vicente, Chem. Mater. 16 (2004) 5721–5725.
[31] D.Z. Liu, W. Hayes, M. Kurmoo, M. Dalton, C. Chen, Physica C 235–240 (1994) 1203–1204.
[32] A.J. Bard, L.R. Faulkner, Electrochemical Methods Fundamentals and Applications, second ed., Wiley, New York, 2001.
[33] W.L. Liu, J.P. Tu, Y.Q. Qiao, J.P. Zhou, S.J. Shi, X.L. Wang, C.D. Gu, J. Power Sources 196 (2011) 7728–7735.